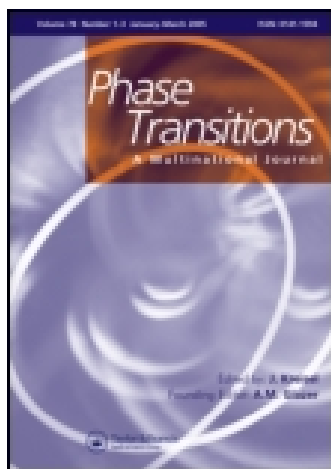


This article was downloaded by: [Simon Fraser University]

On: 13 November 2014, At: 03:03

Publisher: Taylor & Francis

Informa Ltd Registered in England and Wales Registered Number: 1072954 Registered office: Mortimer House, 37-41 Mortimer Street, London W1T 3JH, UK



## Phase Transitions: A Multinational Journal

Publication details, including instructions for authors and subscription information:

<http://www.tandfonline.com/loi/gpht20>

### Simulation of domain patterns in BaTiO<sub>3</sub>

P. Marton<sup>a</sup> & J. Hlinka<sup>a</sup>

<sup>a</sup> Institute of Physics, Academy of Sciences of the Czech Republic , Na Slovance 2, 18221 Praha 8, Czech Republic

Published online: 28 Nov 2010.

To cite this article: P. Marton & J. Hlinka (2006) Simulation of domain patterns in BaTiO<sub>3</sub> , Phase Transitions: A Multinational Journal, 79:6-7, 467-483, DOI: [10.1080/01411590600892351](https://doi.org/10.1080/01411590600892351)

To link to this article: <http://dx.doi.org/10.1080/01411590600892351>

PLEASE SCROLL DOWN FOR ARTICLE

Taylor & Francis makes every effort to ensure the accuracy of all the information (the "Content") contained in the publications on our platform. However, Taylor & Francis, our agents, and our licensors make no representations or warranties whatsoever as to the accuracy, completeness, or suitability for any purpose of the Content. Any opinions and views expressed in this publication are the opinions and views of the authors, and are not the views of or endorsed by Taylor & Francis. The accuracy of the Content should not be relied upon and should be independently verified with primary sources of information. Taylor and Francis shall not be liable for any losses, actions, claims, proceedings, demands, costs, expenses, damages, and other liabilities whatsoever or howsoever caused arising directly or indirectly in connection with, in relation to or arising out of the use of the Content.

This article may be used for research, teaching, and private study purposes. Any substantial or systematic reproduction, redistribution, reselling, loan, sub-licensing, systematic supply, or distribution in any form to anyone is expressly forbidden. Terms & Conditions of access and use can be found at <http://www.tandfonline.com/page/terms-and-conditions>

## Simulation of domain patterns in BaTiO<sub>3</sub>

P. MARTON and J. HLINKA\*

Institute of Physics, Academy of Sciences of the Czech Republic,  
Na Slovance 2, 18221 Praha 8, Czech Republic

(Received 22 May 2006; in final form 16 June 2006)

Computer simulations of domain structure were performed within the continuous phenomenological time-dependent Ginzburg–Landau–Devonshire model including electrostatic long-range interactions. Calculations are done on cube or rectangle area blocks with periodic boundary conditions, employing the previously proposed method consisting in eliminating the elastic field using Euler’s equations and solving the kinetic equations in Fourier space. The authors demonstrate that both strong anisotropy of the Ginzburg gradient interaction and realistic estimation of elastic and electrostatic long-range interactions are crucial for correct domain wall properties of BaTiO<sub>3</sub>-type ferroelectrics. Domain architecture obtained from simulations performed with the authors’ model parameters for BaTiO<sub>3</sub> is found to be in reasonable agreement with experiment.

*Keywords:* BaTiO<sub>3</sub>; Ferroelectric domains; Computer simulation

### 1. Introduction

It is well known that domain structure has enormous impact on the behaviour of ferroelectric materials, and there has been significant progress in systematic attempts to control domain architecture in order to achieve desired material properties. Very basic types and geometrical properties of domain walls and domain structure types in a ferroelectric material can usually be deduced from symmetry, elastic compatibility and electrostatic considerations [1]. For example, this kind of consideration allows one to predict the preferred crystallographic orientations of the 180° and 90° domain boundaries in tetragonal BaTiO<sub>3</sub>, which is one of the classical model materials. In cases of more complex or dense domain wall structure, the analysis can usually be done within the framework of the Ginzburg–Landau–Devonshire model, possibly including electrostatic long-range interactions. Simple tasks, like predicting the domain size in an equilibrium periodic domain slab, the thickness and shape of equilibrium domain walls, the value of polarization in the centre of the domain and so on, can often be done analytically. More complex problems have to be solved numerically, and the framework of the time-dependent Ginzburg–Landau model describing the relaxational evolution of domain structure under specified initial

---

\*Corresponding author. Email: hlinka@fzu.cz

and boundary conditions offers a rather straightforward method with a very clear physics beyond.

Several groups before us tried such time-dependent Ginzburg–Landau computer simulations for multi-component order-parameter ferroelectrics like  $\text{BaTiO}_3$  and different computational strategies were developed to make this task feasible in 2D, or even 3D, regions of reasonable size [2–5]. Unfortunately, certain model parameters of the Ginzburg–Landau potential, such as the coefficients of the gradient interaction, are usually not very well known. Consequently, although there are several previous computer simulations where the choice of model parameters was inspired by  $\text{BaTiO}_3$ , one can hardly expect that these simulations would allow quantitative agreement with observations in the real  $\text{BaTiO}_3$ . Recently, however, we have derived all the missing parameters from the experimental bulk properties of  $\text{BaTiO}_3$  crystals, and the resulting parameter set proved to result in a realistic thickness for both  $180^\circ$  and  $90^\circ$  domain boundaries. The aim of the present paper is to study domain wall architectures with this realistic model.

Our paper is organized as follows. Section 2 introduces the phenomenological model used; section 3 sums up the procedure for eliminating the elastic field; and section 4 describes in detail our method for solving the corresponding time-dependent Ginzburg–Landau equation. Sections 5 and 6 are devoted to the presentation of our results, a brief comparison with other theoretical and experimental results, and to discussion and conclusions.

## 2. Generalized Ginzburg–Landau–Devonshire model

We use the following definition of Ginzburg–Landau free energy of the system:

$$F = F_L^{(e)}\{P_i\} + F_C\{e_{ij}\} + F_q\{P_i, e_{ij}\} + F_G\{P_{i,j}\} + F_{\text{dep}}\{P_i\} \\ = \int d^3r \left[ f_L^{(e)}\{P_i\} + f_C\{e_{ij}\} + f_q\{P_i, e_{ij}\} + f_G\{P_{i,j}\} \right] + F_{\text{dep}}\{P_i\}. \quad (1)$$

Here  $F_L^{(e)}$  is the Landau energy associated with a mechanically clamped system,  $F_G$  is the energy associated with the gradient of polarization,  $F_C$  is purely elastic energy,  $F_q$  describes electrostriction and  $F_{\text{dep}}$  is the electrostatic dipole–dipole interaction.

Individual energy terms depend on the (generally inhomogeneous) polarization field  $\mathbf{P}(\mathbf{r}) = (P_1(\mathbf{r}), P_2(\mathbf{r}), P_3(\mathbf{r}))$ , derivatives of its components  $P_{i,j}(\mathbf{r})$  and on the values of the elastic strain field  $e_{ij}(\mathbf{r})$  defined as

$$e_{ij} = \frac{1}{2}(u_{i,j} + u_{j,i}), \quad (2)$$

where  $u_i$  is the  $i$ th component of the elastic displacement field. Below we also use abbreviated Voigt notation for symmetric tensors  $e_1 = e_{11}$ ,  $e_2 = e_{22}$ ,  $e_3 = e_{33}$ ,  $e_4 = 2e_{23}$ ,  $e_5 = 2e_{13}$  and  $e_6 = 2e_{12}$ . Greek indexes stands for contracted indexes  $\alpha \in \{1, 2, 3, 4, 5, 6\}$ , while Latin symbols  $i, j \in \{1, 2, 3\}$  are indexes of directions in three-dimensional space corresponding to  $x, y, z$ , respectively.

For the sake of clarity, we give below the explicit parametrization of distinct terms of the Ginzburg–Landau excess free energy used in the present calculation.

## 2.1. Landau–Devonshire potential

Recently, it was argued [6, 7] that the Landau energy of BaTiO<sub>3</sub> should be expanded up to eighth order in polarization. In this paper, the mechanically clamped Landau energy (at fixed strain) is thus written as follows:

$$\begin{aligned}
 f_L^{(e)}\{P_i\} = & \alpha_1(P_1^2 + P_2^2 + P_3^2) \\
 & + \alpha_{11}^{(e)}(P_1^4 + P_2^4 + P_3^4) \\
 & + \alpha_{12}^{(e)}(P_1^2 P_2^2 + P_2^2 P_3^2 + P_1^2 P_3^2) \\
 & + \alpha_{111}(P_1^6 + P_2^6 + P_3^6) \\
 & + \alpha_{112}[P_1^4(P_2^2 + P_3^2) + P_2^4(P_1^2 + P_3^2) + P_3^4(P_1^2 + P_2^2)] \\
 & + \alpha_{123}P_1^2 P_2^2 P_3^2 \\
 & + \alpha_{1111}(P_1^8 + P_2^8 + P_3^8) \\
 & + \alpha_{1112}[P_1^6(P_2^2 + P_3^2) + P_2^6(P_1^2 + P_3^2) + P_3^6(P_1^2 + P_2^2)] \\
 & + \alpha_{1122}(P_1^4 P_2^4 + P_2^4 P_3^4 + P_1^4 P_3^4) \\
 & + \alpha_{1123}(P_1^4 P_2^2 P_3^2 + P_2^4 P_1^2 P_3^2 + P_3^4 P_1^2 P_2^2).
 \end{aligned} \tag{3}$$

All corresponding coefficients were recently determined [6]. However, we expect that for present simulations a simpler model with sixth-order expansion, as described for example in [8] would also be quite reasonable. The usual elastic and electrostriction contributions are defined through elastic and electrostriction tensors as follows:

$$\begin{aligned}
 f_C\{e_{ij}\} &= \frac{1}{2}e_\rho C_{\rho\sigma}e_\sigma \\
 &= \frac{1}{2}C_{11}(e_{11}^2 + e_{22}^2 + e_{33}^2) \\
 &\quad + C_{12}(e_{22}e_{33} + e_{11}e_{33} + e_{11}e_{22}) \\
 &\quad + 2C_{44}(e_{23}^2 + e_{13}^2 + e_{12}^2),
 \end{aligned} \tag{4}$$

and

$$\begin{aligned}
 f_q\{P_i, e_{ij}\} &= -q_{11}(e_{11}P_1^2 + e_{22}P_2^2 + e_{33}P_3^2) \\
 &\quad - q_{12}[e_{11}(P_2^2 + P_3^2) + e_{22}(P_1^2 + P_3^2) + e_{33}(P_1^2 + P_2^2)] \\
 &\quad - 2q_{44}(e_{12}P_1P_2 + e_{13}P_1P_3 + e_{23}P_2P_3) \\
 &= -\sum_{\rho=1}^6 e_\rho g_\rho,
 \end{aligned} \tag{5}$$

where  $g_\rho$  are

$$g_1 = (q_{11} - q_{12})P_1^2 + q_{12}(P_1^2 + P_2^2 + P_3^2) \tag{6}$$

$$g_2 = (q_{11} - q_{12})P_2^2 + q_{12}(P_1^2 + P_2^2 + P_3^2) \tag{7}$$

$$g_3 = (q_{11} - q_{12})P_3^2 + q_{12}(P_1^2 + P_2^2 + P_3^2) \tag{8}$$

$$g_4 = q_{44}P_2^2 P_3^2 \tag{9}$$

$$g_5 = q_{44}P_1^2 P_3^2 \tag{10}$$

$$g_6 = q_{44}P_1^2 P_2^2. \tag{11}$$

Electrostrictive coupling implies that the homogeneous equilibrium polarization in the ferroelectric phase depends on the mechanical conditions of the sample. Therefore one has to distinguish the clamped coefficients  $\alpha_{11}^{(e)}$ ,  $\alpha_{12}^{(e)}$  defined above from the stress-free coefficients  $\alpha_{11}$ ,  $\alpha_{12}$  appearing in the Landau potential of a stress-free sample. They are related through elastic and electrostrictive tensors as shown for example in [4, 9, 10].

## 2.2. Non-local interactions

We assume that polarizations  $P_1(\mathbf{r})$ ,  $P_2(\mathbf{r})$ ,  $P_3(\mathbf{r})$  are continuous functions of position up to second derivatives. Lowest order (weakly) non-local interaction is described as usual by a quadratic form in polarization gradients

$$\begin{aligned} f_G\{P_{i,j}\} = & \frac{1}{2}G_{11}(P_{1,1}^2 + P_{2,2}^2 + P_{3,3}^2) \\ & + G_{14}(P_{1,1}P_{2,2} + P_{2,2}P_{3,3} + P_{1,1}P_{3,3}) \\ & + \frac{1}{2}G_{44}(P_{1,2}^2 + P_{2,1}^2 + P_{2,3}^2 + P_{3,2}^2 + P_{3,1}^2 + P_{1,3}^2). \end{aligned} \quad (12)$$

To describe the electrostatic effects associated with the inhomogeneity of the polarization field, it is important to include the additional, strongly non-local term

$$F_{\text{dep}}\{P_i\} = \frac{1}{8\pi\epsilon_0\epsilon_B} \iint d^3r d^3s \left[ \frac{\mathbf{P}(\mathbf{r}) \cdot \mathbf{P}(\mathbf{s})}{|\mathbf{R}|^3} - \frac{3[\mathbf{P}(\mathbf{r}) \cdot \mathbf{R}][\mathbf{P}(\mathbf{s}) \cdot \mathbf{R}]}{|\mathbf{R}|^5} \right] \quad (13)$$

describing the long-range interaction of individual dipoles with the electric fields of all other dipoles. Here  $\epsilon_B$  stands for the relative permittivity of the background, coming from electron polarizability and from contributions of higher frequency polar phonon modes and  $\mathbf{R} = \mathbf{r} - \mathbf{s}$ . Let us note that we will use periodic boundary conditions so that there is no depolarization energy associated with surface charges on these boundaries, as is the case with infinite bulk or samples with ideal short-cut boundary conditions.

## 2.3. Model parameters

In this work, two sets of parameter values are used (see table 1). Parameter set A was derived in a recent independent work (parameter set III quoted in [10]). For example, the gradient term coefficients and the value of  $\epsilon_B$  were determined from available inelastic neutron scattering and infrared reflectivity investigations of bulk BaTiO<sub>3</sub>, and the Landau potential corresponding to a stress-free and homogeneously polarized sample is in this case the same as the Landau energy of recent reference [6] at 298 K.

The parameter set B is derived from the model described in [3]. The mentioned work [3] uses only dimensionless parameters, re-scaled with the help of auxiliary quantities derived from parameters  $\alpha_1$ ,  $G_{11}$  and the clamped equilibrium spontaneous polarization  $P_0^{(e)}$ . For a closer comparison,  $\alpha_1$ ,  $G_{11}$  are taken from the parameter set A,  $P_0^{(e)} \approx 0.26 \text{ C m}^{-2}$ , and the remaining parameters are reconstructed from the dimensionless values given in table 1 of [3], using the re-scaling procedure defined there (equations 43–44 of [3]). (Let us note that the parameters  $\alpha_{11}$  and  $\alpha_{12}$  obviously correspond to our clamped values  $\alpha_{11}^{(e)}$ ,  $\alpha_{12}^{(e)}$ .) This straightforward procedure gives completely the wrong order of magnitude for the elastic and electrostrictive tensors.

Table 1. Complete list of parameters describing the phenomenological model defined in section 2. The set of numerical values ‘A’ corresponds to realistic room temperature BaTiO<sub>3</sub> derived in [10]. Set ‘B’ is derived from re-scaled values of [3] as explained in the text.

	A	B	Unit (SI)
$\alpha_1$	-3.712	-3.712	$10^7 \text{ J m C}^{-2}$
$\alpha_{11}$	-2.097	-2.790	$10^8 \text{ J m}^5 \text{ C}^{-4}$
$\alpha_{11}^{(e)}$	6.079	-2.745	$10^8 \text{ J m}^5 \text{ C}^{-4}$
$\alpha_{12}$	7.974	49.45	$10^8 \text{ J m}^5 \text{ C}^{-4}$
$\alpha_{12}^{(e)}$	1.303	49.41	$10^8 \text{ J m}^5 \text{ C}^{-4}$
$\alpha_{111}$	1.294	6.497	$10^9 \text{ J m}^{-9} \text{ C}^{-6}$
$\alpha_{112}$	-1.950	32.48	$10^9 \text{ J m}^{-9} \text{ C}^{-6}$
$\alpha_{123}$	-2.500	8.121	$10^9 \text{ J m}^{-9} \text{ C}^{-6}$
$\alpha_{1111}$	3.863	—	$10^{-10} \text{ J m}^{-13} \text{ C}^{-8}$
$\alpha_{1112}$	2.529	—	$10^{-10} \text{ J m}^{-13} \text{ C}^{-8}$
$\alpha_{1122}$	1.637	—	$10^{-10} \text{ J m}^{-13} \text{ C}^{-8}$
$\alpha_{1123}$	1.367	—	$10^{-10} \text{ J m}^{-13} \text{ C}^{-8}$
$G_{11}$	51	51	$10^{-11} \text{ J m}^3 \text{ C}^{-2}$
$G_{14}$	0	0	$10^{-11} \text{ J m}^3 \text{ C}^{-2}$
$G_{44}$	2	51	$10^{-11} \text{ J m}^3 \text{ C}^{-2}$
$q_{11}$	14.20	0.00527	$10^9 \text{ J m C}^{-2}$
$q_{12}$	-0.74	-0.000275	$10^9 \text{ J m C}^{-2}$
$q_{44}$	1.57	0.000582	$10^9 \text{ J m C}^{-2}$
$C_{11}$	27.50	0.000690	$10^{-10} \text{ J m}^{-3}$
$C_{12}$	17.90	0.000449	$10^{-10} \text{ J m}^{-3}$
$C_{44}$	5.43	0.000135	$10^{-10} \text{ J m}^{-3}$
$\epsilon_B$	7.35	1	

These parameters arise in the simulations only through the effective elasto-electrostrictive energy (derived in the next section), which happens to be about two orders of magnitude lower than in parameter set A. Nevertheless, we have used this parameter set for comparison, too.

### 3. Effective long-range elastic interaction

The above defined Ginzburg–Landau–Devonshire potential acts upon polarization and strain fields. Strain plays the role of a secondary order parameter and it can be written as the sum of the homogeneous macroscopic strain and heterogeneous strain components (with zero spatial average). The average strain is usually controlled by macroscopic boundary conditions. For example, the natural condition for a ferroelectric grain in a dense bulk ceramic can be fixed stress, while a free-standing single crystal might be assumed in the stress-free state. We will assume here that the system is macroscopically clamped, i.e. we will not consider the term associated with changes of the average strain. The heterogeneous part of the elastic strain field is usually eliminated assuming that its relaxation towards mechanical equilibrium is much faster than the evolution of the inhomogeneities of the polarization field [2].

In this case, the heterogeneous strain is determined from the local mechanical equilibrium conditions given by the Euler–Lagrange equation

$$\sum_{j=1}^3 \frac{\partial \sigma_{ij}}{\partial x_j} = \sum_{j=1}^3 \frac{\partial}{\partial x_j} \left( \frac{\partial F}{\partial u_{ij}} \right) = 0, \quad (14)$$

where  $\sigma_{ij}$  is the local stress field. Elimination of the heterogeneous strain is conveniently done using the Fourier transform of  $u_i$  and  $g_{ij}$

$$\mathcal{F}(u_i) = u_i(\mathbf{k}) = \frac{1}{(2\pi)^{3/2}} \int d^3r [u_i(\mathbf{r}) \exp(-i\mathbf{k} \cdot \mathbf{r})] \quad (15)$$

$$\mathcal{F}(g_{ij}) = g_{ij}(\mathbf{k}) = \frac{1}{(2\pi)^{3/2}} \int d^3r [g_{ij}(\mathbf{r}) \exp(-i\mathbf{k} \cdot \mathbf{r})] \quad (16)$$

by the procedure described for example in [4], in which the Fourier components of the instantaneous equilibrium strain field are expressed via the Fourier components of the electrostrictive tensile stress field  $g_{ij}(\mathbf{r})$  and the directional cosines  $\hat{\mathbf{k}} = \mathbf{k}/|\mathbf{k}|$  as follows:

$$u_j(\mathbf{k}) = -\frac{i}{k} \left[ \frac{G_j(\mathbf{k})}{d_j} - \frac{D(\hat{\mathbf{k}})H(\mathbf{k})\hat{k}_j}{d_j} \right], \quad (17)$$

where

$$G_i(\mathbf{k}) = \sum_{j=1}^3 \hat{k}_j g_{ij}(\mathbf{k}), \quad (18)$$

$$H(\mathbf{k}) = \sum_{i=1}^3 \hat{k}_i G_i(\mathbf{k})/d_i, \quad (19)$$

$$D(\hat{\mathbf{k}}) = (C_{12} + C_{44}) \left[ 1 + (C_{12} + C_{44}) \chi(\hat{\mathbf{k}}) \right], \quad (20)$$

$$\chi(\hat{\mathbf{k}}) = \sum_i \hat{k}_i^2 / d_i, \quad (21)$$

$$d_i(\hat{\mathbf{k}}) = C_{44} (1 + \xi \hat{k}_i^2), \quad (22)$$

$$\xi = (C_{11} - C_{12} - 2C_{44})/C_{44}. \quad (23)$$

After substitution of the back Fourier-transformed elastic displacement field into the expression for the electrostriction and elastic energies, we finally get the ‘elasto-striction’ energy

$$F_{\text{Cq}} = F_{\text{C}} + F_{\text{q}} = -\frac{1}{2} \sum_{\rho} \sum_{\sigma} \int d^3k \left[ \mathbf{B}_{\rho\sigma}(\hat{\mathbf{k}}) g_{\rho}(\mathbf{k}) g_{\sigma}(-\mathbf{k}) \right], \quad (24)$$

where the  $\mathbf{B}(\hat{\mathbf{k}})$  matrix reads

$$B_{\rho\sigma}(\hat{\mathbf{k}}) = \beta_{\rho\sigma}(\hat{\mathbf{k}}) - D(\hat{\mathbf{k}}) \theta_{\rho}(\hat{\mathbf{k}}) \theta_{\sigma}(\hat{\mathbf{k}}), \quad (25)$$

and where matrix elements  $\beta_{\rho\sigma}$  given explicitly in [4], depend on directional cosines only (see also [11]).

Once the  $F_C\{e_{ij}\} + F_q\{P_i, e_{ij}\}$  terms in the Ginzburg–Landau–Devonshire free energy functional are replaced by the above expression for quasi-equilibrium elastostriiction energy  $F_{Cq}\{P_i\}$ , the total Gibbs free energy depends on polarization field only (and we will denote it as  $F'$ ). The long-range nature of elastostriictive interaction appears after transformation from Fourier space to the direct space [4]

$$F_{Cq} = -\frac{1}{2} \int \int d\mathbf{r}_1 d\mathbf{r}_2 \sum_{\rho=1}^6 \sum_{\sigma=1}^6 \Psi_{\rho\sigma}(\mathbf{r}_2 - \mathbf{r}_1) Y_{\rho}(\mathbf{r}_1) Y_{\rho}(\mathbf{r}_2), \quad (26)$$

where  $\Psi_{\rho\sigma}$  is the back Fourier transform of kernels  $A_{\rho\sigma}$ , which are linear combinations of  $B_{\rho\sigma}$ ;

$$\Psi_{\rho\sigma}(\mathbf{R}) = \frac{1}{(2\pi)^d} \int d\mathbf{k} A_{\rho\sigma}(\hat{\mathbf{k}}) \exp(-i\mathbf{k} \cdot \mathbf{R}). \quad (27)$$

Definitions of the vector  $\mathbf{Y}$  is defined as  $\mathbf{Y} = [P_1^2, P_2^2, P_3^2, P_2P_3, P_1P_3, P_1P_2]$ .

#### 4. Time-dependent Ginzburg–Landau equation in Fourier space

We shall assume that the evolution of the system is driven by the usual dissipative time-dependent Ginzburg–Landau equation

$$\frac{\partial}{\partial t} P_i(\mathbf{r}, t) = -\Lambda \frac{\delta F'}{\delta P_i}(\mathbf{r}, t) + \xi_i(\mathbf{r}, t), \quad (28)$$

where  $\Lambda$  is the kinetic coefficient (set arbitrarily to  $\Lambda = 1 \text{ kg}^{-1} \text{ m}^{-3} \text{ s C}^2$ ) and  $\xi_i(\mathbf{r}, t)$  stands for random force of fluctuations, which is omitted in the present simulation. In principle, the time evolution of the  $P_i(\mathbf{r})$  field can be calculated straightforwardly from this equation, but in the case of periodic boundary conditions it is convenient to solve an equivalent equation [3] for the Fourier components of  $P_i(\mathbf{r})$

$$\frac{\partial}{\partial t} \mathcal{F}[P_i(\mathbf{r})](\mathbf{k}, t) = -\Lambda \mathcal{F}\left[\frac{\delta F'}{\delta P_i}(\mathbf{r})\right](\mathbf{k}, t), \quad (29)$$

since applying the discrete Fourier transformation greatly simplifies numerical calculations of the long-range forces. This approach requires evaluation of the Fourier transforms of the functional derivative on the right-hand side of the above equation:

$$\mathcal{F}\left[\frac{\delta F'}{\delta P_i}\right] = \mathcal{F}\left[\frac{\delta F_L^{(e)}}{\delta P_i}\right] + \mathcal{F}\left[\frac{\delta F_G}{\delta P_i}\right] + \mathcal{F}\left[\frac{\delta F_{Cq}}{\delta P_i}\right] + \mathcal{F}\left[\frac{\delta F_{\text{dep}}}{\delta P_i}\right]. \quad (30)$$

Explicit expressions used in the calculation of this generalized force are derived in the Appendix. Obviously, these expressions are equally valid for the 3D discrete Fourier transformation

$$\mathcal{F}_d[f(\mathbf{r}_d)](\mathbf{k}_d) = \frac{1}{\sqrt{R_1 R_2 R_3}} \sum_{\substack{r_m=0 \\ m \in \{1, 2, 3\}}}^{R_m-1} f(\mathbf{r}_d) \exp\left[2\pi i \sum_{n=1}^3 k_n \frac{r_n}{R_n}\right], \quad (31)$$



which is used instead of the original non-periodic Fourier transform  $\mathcal{F}(\mathbf{r}_d, \mathbf{k}_d)$  stand for ‘discrete’ points in direct and Fourier space, respectively, and  $R_n$  is the number of discrete points in a particular direction).

Two-dimensional simulations in this paper actually represent 3D material with no order parameter variation along the  $z$ -axis and with  $P_3 = 0$ ,  $u_3 = 0$ . The Landau, gradient, elastostrictive and dipole–dipole parts of the acting forces are then calculated using the same formulas, simplified merely by setting  $P_3 = 0$ ; 3D Fourier transformations can be replaced by 2D ones, i.e.

$$\mathcal{F}_d^{2D}[f(\mathbf{r}_d)](\mathbf{k}_d) = \frac{1}{\sqrt{R_1 R_2}} \sum_{\substack{r_m=0 \\ m \in \{1, 2\}}}^{R_m-1} f(\mathbf{r}_d) \exp \left[ 2\pi i \sum_{n=1}^2 k_n \frac{r_n}{R_n} \right]. \quad (32)$$

The time-dependent Ginzburg–Landau equation in Fourier space is solved in this work by the most simple method, i.e. the first-order Euler scheme. In every step, the generalized force acting at each particular reciprocal point is computed and consequently the value of the corresponding Fourier component is changed according to the discretized time-dependent Ginzburg–Landau equation in reciprocal space

$$\mathcal{F}_d[P_i](\mathbf{k}_d, t + \tau) = \mathcal{F}_d[P_i](\mathbf{k}_d, t) - \tau \Lambda \mathcal{F}_d \left[ \frac{\delta F'}{\delta P_i} \right](\mathbf{k}_d, t), \quad (33)$$

with time step  $\tau$  and equidistant division of the spatial domain corresponding to the real-space step  $\Delta$ . Requirements on the  $\tau$  and  $\Delta$  relation in order to get a stable method are the same as if the simulation had taken place in real space.

It is quite straightforward to increase the order of the numerical scheme, but it does not remove the greatest disadvantages of the present method, i.e. mutual interdependence of the time and spatial steps and possible instability of the scheme. Implementation of an implicit method is difficult owing to the high nonlinearity. Possible improvement using the semi-implicit scheme proposed in [3, 12] allows one to increase the time step considerably, but it was not applied in this work. In any case we have checked numerically with the half-step method that the error in the final results of the present simulations is not essential.

## 5. Results

Probably the most remarkable achievement in computer simulations of domain structure formation in BaTiO<sub>3</sub>-type materials is the 3D simulation of [3], performed with the mentioned semi-implicit Fourier-spectral method. For the sake of comparison, we first present closely analogous simulations with the model of [3] (using parameter set B), and then we proceed to results obtained with the improved model, tailored for room-temperature BaTiO<sub>3</sub> (using parameter set A).

The graphical scheme used for the decoration of ferroelectric domains appearing in displayed polarization fields is apparent from figure 1. In 2D simulations with the polarization restricted to the plane of the figure, the local polarization direction is represented by tiny arrows and shading code (enlarged figure 1a); the size of the arrows is proportional to the modulus of the polarization vector. Results of three-dimensional simulations are shown by two-dimensional cuts and the same arrow/shading scheme is used for the in-plane component of the polarization vector, provided that the normal component is the smaller. The local polarization

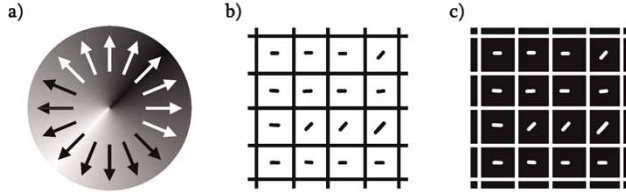


Figure 1. Graphical code used for decoration of ferroelectric domains. (a) Polarization in plane of the figure. (b) Region with polarization up. (c) Region with polarization down.

perpendicular to the plane of the plot (or when the angle between  $\mathbf{P}$  and the plane normal is smaller than  $45^\circ$ ) is represented by circumscribed square tiles (white tiles for polarization up and black tiles for polarization down); arrows indicating the eventual residual in-plane component are replaced by short contrast segments (enlarged in figure 1b, c).

In all cases our simulation started from small random noise, equally distributed in range  $< -0.01P_0, 0.01P_0 >$ . The discrete time step was  $\tau = 10^{-10}$  s, but it should not be considered as real time unless it is later corrected with the true value of the kinetic coefficient  $\Lambda$ .

### 5.1. Simulations with parameter set B

The domain patterns displayed in figure 2 should be in principle quite analogous to those of figure 2 of [3]. Indeed, parameter set B was calculated from the reduced parameter values of [3], our lattice spacing corresponds to a single reduced unit of [3] ( $\Delta = \sqrt{G_{11}}/|\alpha_1| \approx 3.7$  nm); the size of the 3D simulation box was identical ( $64 \times 64 \times 64$  lattice grid) and both simulations were started from the paraelectric state (in our case, from a small amplitude noise described above). For numerical reasons, we could not use the same time step (equivalent to  $0.05/(|\alpha_1|\Lambda) \approx 1.35$  ns), but the number of steps  $N$  was increased so that the simulation duration in reduced time units ( $N\Delta|\alpha_1|\Lambda$ ) was identical.

In agreement with [3], we have observed all six possible domain states corresponding to the tetragonal phase of BaTiO<sub>3</sub>, with domains of similar size and separated primarily by head-to-tail  $90^\circ$  domain walls. The speed of evolution is similar, and the domain wall thicknesses are also similar. However, in contrast with the results of [3], there are also few residual  $180^\circ$  domain walls and the domains seem to have slightly different shapes.

These differences suggest that we unfortunately do not have equivalent model parameters. First of all, there is probably a missprint in table 1 of [3], since the re-scaled parameter values are not consistent (the minimum of the re-scaled potential is not at  $P_0 = 1$ ). We have realized that it can be corrected, for instance, by taking  $\alpha'_{11} = -0.7$  instead of  $\alpha'_{11} = -0.5$ , but the values of the elastic and electrostriction coefficients indicate that there is another problem with the re-scaling, which we could not disentangle.

It is nevertheless instructive to perform 2D simulation with the parameter set B, i.e. assuming a  $z$ -independent polarization field with  $P_3 = 0, u_3 = 0$ . The results of such simulations on  $128 \times 128$  grids are shown in figure 3 for equivalent

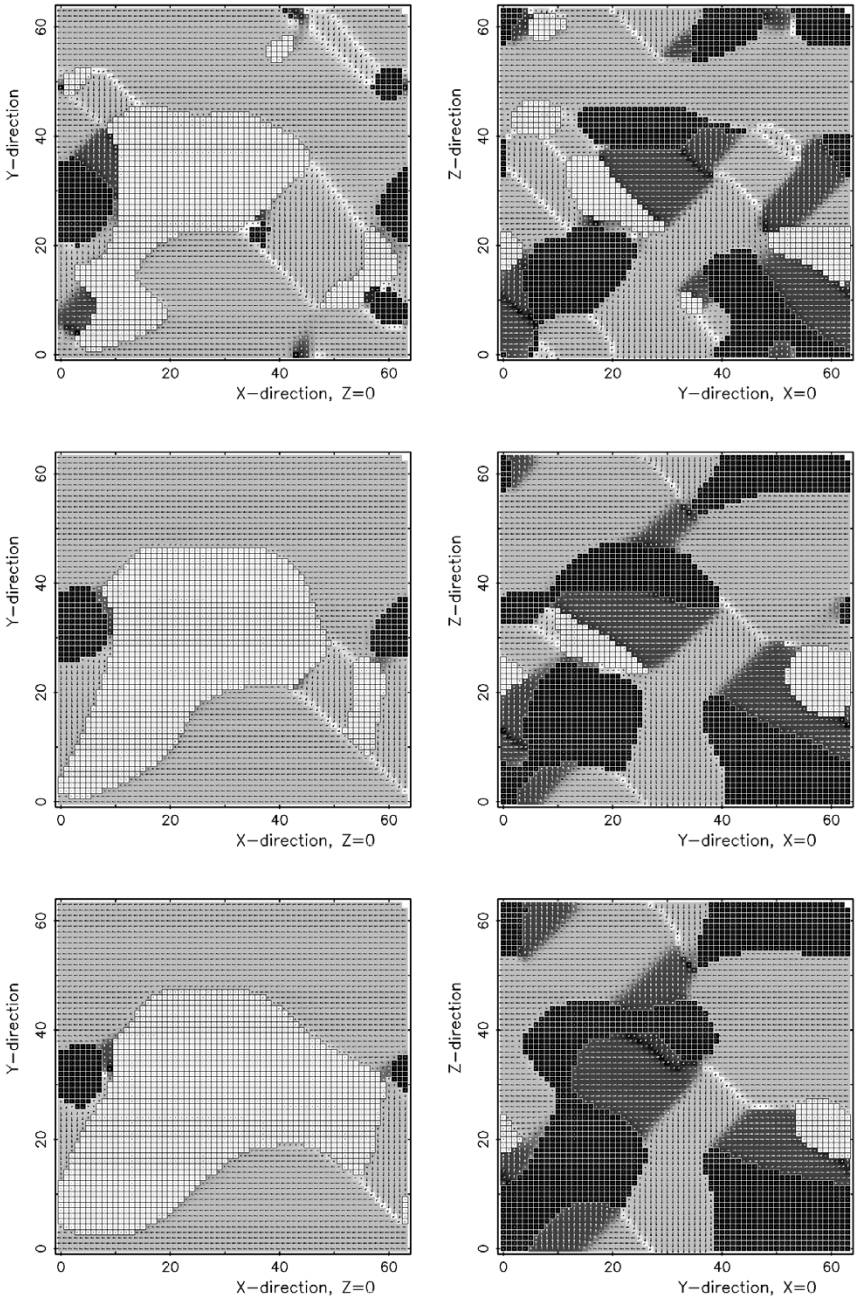


Figure 2. Polarization pattern on  $xy$  (left) and  $yz$  (right) sections through three-dimensional simulation analogous to that of figure 2 of [3] (using parameter set B). From top to bottom, the simulation time corresponds to 500, 1500 and 3000 steps of the cited work.

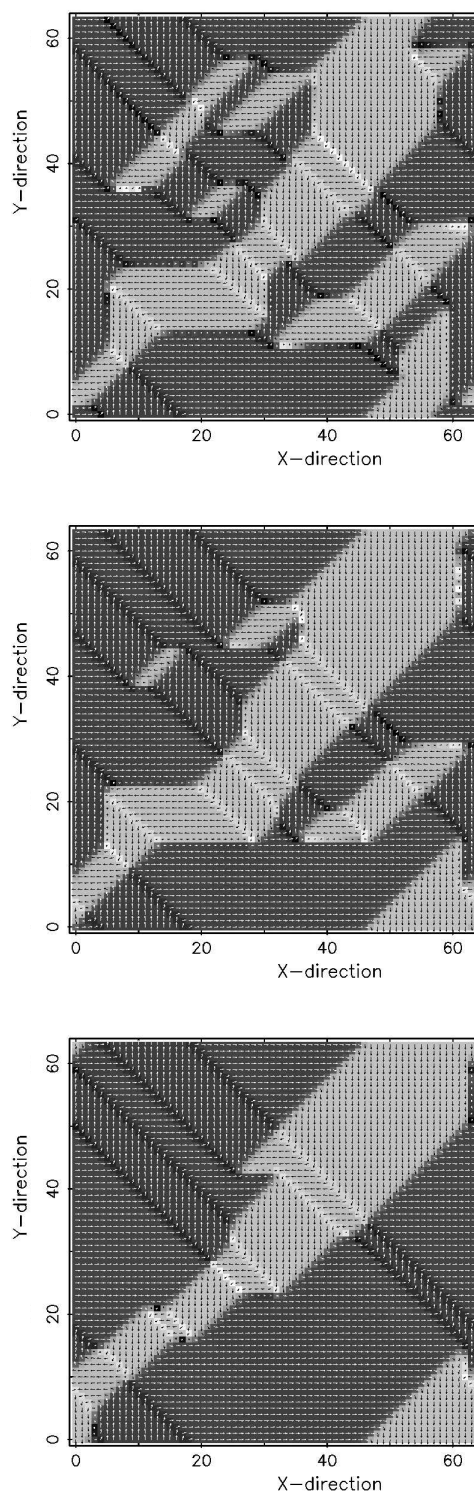


Figure 3. ‘Two-dimensional’ simulations with same parameters and simulation time as in figure 2.



simulation times. It is obvious that relaxation towards an optimized twin structure with (110) type planar head-to-tail ferroelastic domain walls proceeds much faster. Clearly, one can considerably decrease the computation time if the searched for domain pattern is known to have such quasi-2D character. As in the corresponding 3D simulation, there are only very few residual  $180^\circ$  domain walls.

## 5.2. Simulations with parameter set A

Parameter set A was tailored as a quantitative model for room-temperature  $\text{BaTiO}_3$  crystal, and simulated domain patterns with the complete model are thus expected to be quite realistic. To illustrate the role of distinct interactions, we first take into account only the Landau and gradient energy  $f_L^{(e)} + f_G$ . As shown on the left side of figure 4, our choice of the highly anisotropic gradient tensor  $G_{ij}$  produces strong anisotropy in the domain shapes and domain wall orientations. Inside domains, polarization is aligned along  $[110]$  directions, because the minima of the mechanically clamped Landau potential correspond to the orthorhombic state. When the elasto-electrostrictive interaction is added (right side of figure 4), correct tetragonal domain states are formed. Actually obtained domain architecture with coexistence of elastically compatible  $90^\circ$  and  $180^\circ$  domain walls appears already almost realistic. However, some of these domain walls would be charged, as for example the tail-to-tail  $90^\circ$  domain wall indicated by the arrow in the bottom-right corner of figure 4. Such domain walls are obviously suppressed in the full model, which also includes the dipole–dipole electrostatic contribution (left side of figure 5). As the elasto-electrostrictive and dipole–dipole energies are roughly comparable in models defined in parameter sets A and B, we can deduce that the essential contribution which keeps  $180^\circ$  domain walls in simulated patterns is the anisotropic gradient energy. This is confirmed in the simulation shown in the right side of figure 5, which is done for the full model with parameter set A but with  $G_{44}$  set equal to  $G_{11}$ . Indeed, here the  $180^\circ$  domain walls are again suppressed, as in [3] or in our simulations with parameter set B.

## 6. Discussion and conclusion

The domain patterns given in this paper were calculated in the framework of the generalized time-dependent Ginzburg–Landau model, which includes two types of long-range force – elasto-electrostrictive and electrostatic dipole–dipole. It is known that both play a major role in the formation of the domain structures observed in experiments. The A-set of model parameters used in this work was determined from the bulk properties of  $\text{BaTiO}_3$ , and we expect that it should allow predictions for plausible domain architectures of room-temperature  $\text{BaTiO}_3$  crystals. Obviously, domain sizes in the present simulation do not correspond to the typical domain sizes observed in macroscopic samples. Nevertheless, it is expected that the pattern would further coarsen in time while keeping essentially the same morphology, so that the architecture of images can be compared with macroscopic experiments.

As far as we could judge, the observed domain structure images are indeed quite similar to our simulations—they usually show two interpenetrating systems of  $90^\circ$  and  $180^\circ$  charge-neutral domain walls, both obeying elastic compatibility and with somewhat larger densities of  $180^\circ$  species [13, 14]. We have shown that the description of the delicate balance between  $90^\circ$  and  $180^\circ$  domain walls in  $\text{BaTiO}_3$  requires

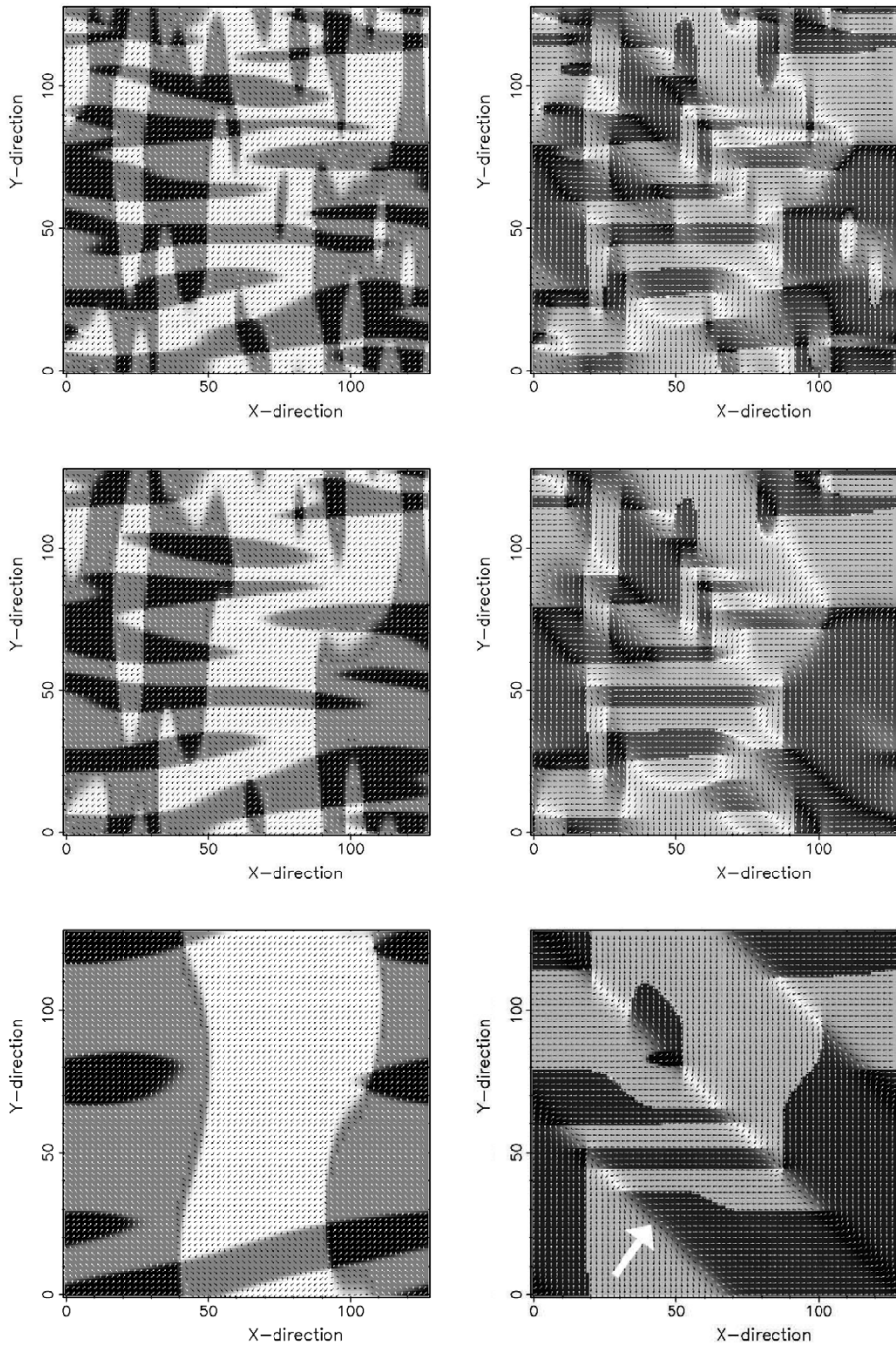


Figure 4. Polarization patterns from 2D simulations using parameter set A. Left: model with only Landau and gradient energy  $f_L^{(e)} + f_G$ . Right: complete model, but *without dipole-dipole interaction*. Arrow indicates charged domain wall. From top to bottom, the simulation time corresponds to 2000, 4000 and 20 000 steps.



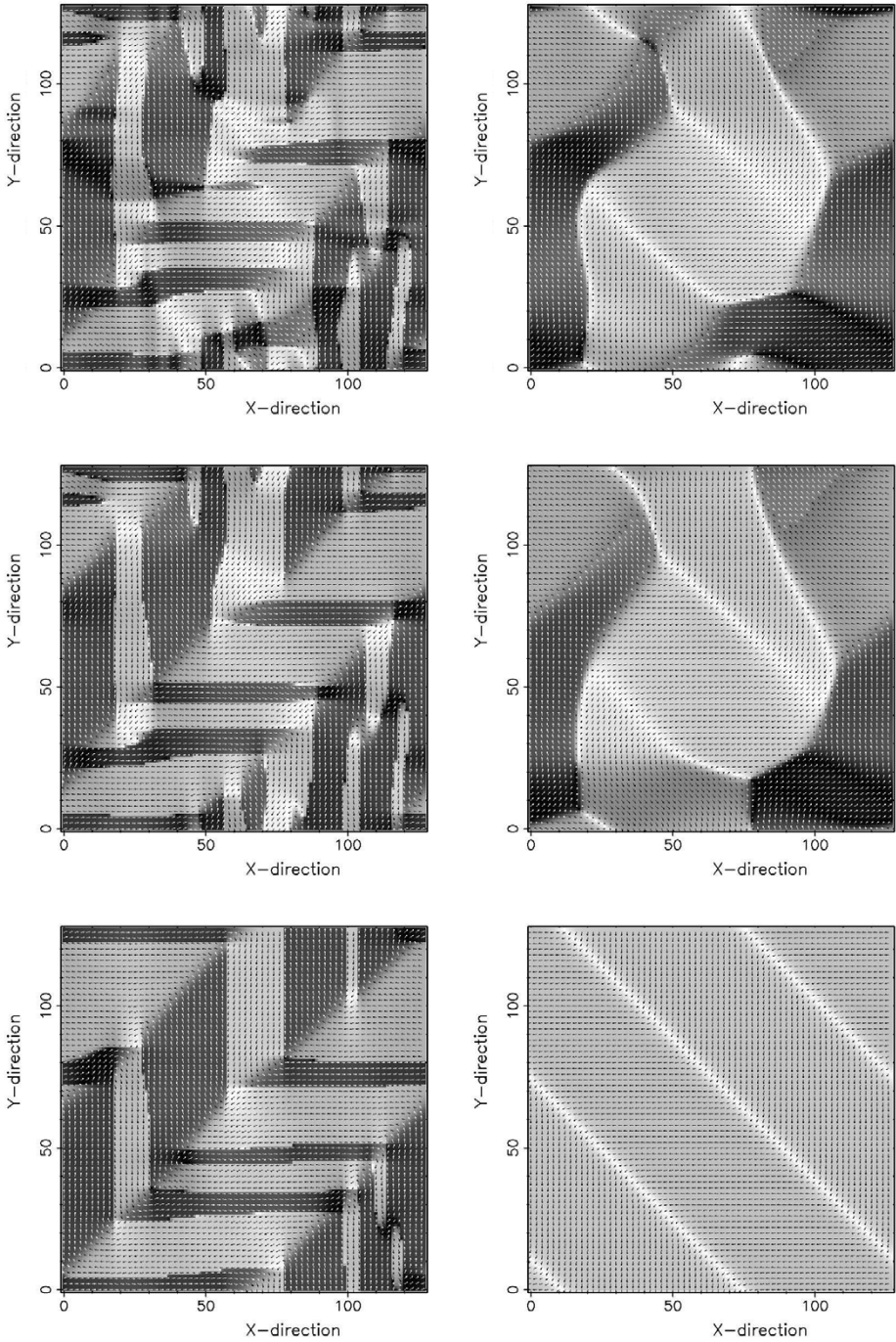


Figure 5. Polarization patterns from 2D simulations using parameter set A. Left: complete model. Right: complete model with *isotropic gradient energy* ( $G_{44} = G_{11}$ ). From top to bottom, the simulation time corresponds to 2000, 4000 and 20000 steps.

not only correct appreciation of long-range forces, but also realistic description of the anisotropy of the short-range gradient term.

### Acknowledgement

This work has been supported by the Grant Agency of the Czech Republic (projects 202/05/H003 and 202/06/0411).

### References

- [1] J. Fousek and V. Janovec, J. Appl. Phys. **40** 135 (1969).
- [2] H.L. Hu and L.Q. Chen, Mater. Sci. Eng. **A238** 182 (1997).
- [3] H.L. Hu and L.Q. Chen, J. Am. Ceram. Soc. **81** 492 (1998).
- [4] S. Nambu and D.A. Sagala, Phys. Rev. B **50** 5838 (1994).
- [5] R. Ahluwalia, T. Lookman, A. Saxena, *et al.*, cond-mat/0308232 (2003).
- [6] Y.L. Li, L.E. Cross and L.Q. Chen, J. Appl. Phys. **98** 064101 (2005).
- [7] Y.L. Wang, A.K. Tagantsev, D. Damjanovic, *et al.*, Phys. Rev. B **73** 132103 (2006).
- [8] A.J. Bell, J. Appl. Phys. **89** 3907 (2001).
- [9] A.F. Devonshire, Phil. Mag. **40** 1040 (1940).
- [10] J. Hlinka and P. Marton, paper presented at the XVIIth Czech–Polish seminar ‘Structural and ferroelectric phase transition’, Znojmo, Czech Republic, 22–26 May (2006).
- [11] J. Hlinka and E. Klotins, J. Phys. Cond. Mat. **15** 5755 (2003).
- [12] L.Q. Chen and J. Shen, Comput. Phys. Commun. **108** 147 (1997).
- [13] L.M. Eng, M. Abplanalp and P. Gunter, Appl. Phys. A **66** S679 (1998).
- [14] M. Abplanalp, L.M. Eng and P. Gunter, Appl. Phys. A **66** S231 (1998).

### Appendix A: functional derivatives of the model potential

#### A.1. Landau force

The functional derivative of the Landau energy functional reads as follows (other components can be obtained by cyclic permutation  $1 \rightarrow 2, 2 \rightarrow 3, 3 \rightarrow 1$ ):

$$\begin{aligned} \frac{\delta F_L^{(e)}\{P_i\}}{\delta P_1} = & P_1 \left\{ 2\alpha_1 + 4\alpha_{11}P_1^2 + 2\alpha_{12}(P_2^2 + P_3^2) + 6\alpha_{111}P_1^4 \right. \\ & + 2\alpha_{112}[P_2^4 + P_3^4 + 2P_1^2(P_2^2 + P_3^2)] + 2\alpha_{123}P_2^2P_3^2 \\ & + 8\alpha_{1111}P_1^6 + 2\alpha_{1112}[P_2^6 + P_3^6 + 3P_1^4(P_2^2 + P_3^2)] \\ & \left. + 4\alpha_{1122}P_1^2(P_2^4 + P_3^4) + 2\alpha_{1123}[2P_1^2P_2^2P_3^2 + P_2^2P_3^2(P_2^2 + P_3^2)] \right\}. \quad (\text{A1}) \end{aligned}$$

The Fourier image of multiplication is equal to the convolution of Fourier images, so we rather use back-transformation of  $P_i(\mathbf{k})$  to the direct space and perform multiplications there. In the end, forward Fourier is used to transform the Landau force into the reciprocal space:

$$\begin{aligned} \mathcal{F}_d \left[ \frac{\delta F_L^{(e)}\{P_i\}}{\delta P_1} \right] = & \mathcal{F}_d \left[ \mathcal{F}_d^{-1}[P_1] \left[ 2\alpha_1 + 4\alpha_{11}(\mathcal{F}_d^{-1}[P_1])^2 \right. \right. \\ & \left. \left. + 2\alpha_{12}[(\mathcal{F}_d^{-1}[P_2])^2 + (\mathcal{F}_d^{-1}[P_3])^2] + \dots \right] \right]. \quad (\text{A2}) \end{aligned}$$



### A.2. Gradient force

The functional derivative of the gradient energy functional in direct space can be derived (using per-partes integration) as follows:

$$\frac{\delta F_G\{P_{i,j}\}}{\delta P_1} = -G_{11}P_{1,11} - G_{14}(P_{2,21} + P_{3,31}) - G_{44}(P_{1,22} + P_{1,33}). \quad (\text{A3})$$

The Fourier-transformed gradient force then reads

$$\mathcal{F}_d \left[ \frac{\delta F_G\{P_{i,j}\}}{\delta \mathbf{P}} \right] = \mathbf{G}\mathbf{P}, \quad (\text{A4})$$

where  $\mathbf{G}$  is a matrix with the following elements:

$$\begin{pmatrix} G_{11}k_1^2 + G_{44}(k_2^2 + k_3^2) & G_{14}k_1k_2 & G_{14}k_1k_3 \\ G_{14}k_1k_2 & G_{11}k_2^2 + G_{44}(k_1^2 + k_3^2) & G_{14}k_2k_3 \\ G_{14}k_1k_3 & G_{14}k_2k_3 & G_{11}k_3^2 + G_{44}(k_1^2 + k_2^2) \end{pmatrix}. \quad (\text{A5})$$

### A.3. Elastostriuctive force

To avoid direct-space convolutions with kernels  $\Psi_{\rho\sigma}$  (26), the whole calculation is performed with its Fourier image  $A_{\rho\sigma}$  (equation 27). It is worth noting that, thanks to its definitions in [4], kernel  $A_{\rho\sigma}$  is symmetric ( $A_{\rho\sigma} = A_{\sigma\rho}$ ).

$$\begin{aligned} \mathcal{F}_d \left[ \frac{\delta F_{Cq}\{P_i\}}{\delta P_1} \right] &= -\frac{1}{2} \mathcal{F}_d \left[ 4P_1 \mathcal{F}_d^{-1} \left[ \sum_{\sigma=1}^6 A_{1\sigma} \mathcal{F}_d[Y_\sigma] \right] + 2P_2 \mathcal{F}_d^{-1} \left[ \sum_{\sigma=1}^6 A_{6\sigma} \mathcal{F}_d[Y_\sigma] \right] \right. \\ &\quad \left. + 2P_3 \mathcal{F}_d^{-1} \left[ \sum_{\sigma=1}^6 A_{5\sigma} \mathcal{F}_d[Y_\sigma] \right] \right], \end{aligned} \quad (\text{A6})$$

$$\begin{aligned} \mathcal{F}_d \left[ \frac{\delta F_{Cq}\{P_i\}}{\delta P_2} \right] &= -\frac{1}{2} \mathcal{F}_d \left[ 4P_2 \mathcal{F}_d^{-1} \left[ \sum_{\sigma=1}^6 A_{2\sigma} \mathcal{F}_d[Y_\sigma] \right] + 2P_3 \mathcal{F}_d^{-1} \left[ \sum_{\sigma=1}^6 A_{4\sigma} \mathcal{F}_d[Y_\sigma] \right] \right. \\ &\quad \left. + 2P_1 \mathcal{F}_d^{-1} \left[ \sum_{\sigma=1}^6 A_{6\sigma} \mathcal{F}_d[Y_\sigma] \right] \right], \end{aligned} \quad (\text{A7})$$

$$\begin{aligned} \mathcal{F}_d \left[ \frac{\delta F_{Cq}\{P_i\}}{\delta P_3} \right] &= -\frac{1}{2} \mathcal{F}_d \left[ 4P_3 \mathcal{F}_d^{-1} \left[ \sum_{\sigma=1}^6 A_{3\sigma} \mathcal{F}_d[Y_\sigma] \right] + 2P_1 \mathcal{F}_d^{-1} \left[ \sum_{\sigma=1}^6 A_{5\sigma} \mathcal{F}_d[Y_\sigma] \right] \right. \\ &\quad \left. + 2P_2 \mathcal{F}_d^{-1} \left[ \sum_{\sigma=1}^6 A_{4\sigma} \mathcal{F}_d[Y_\sigma] \right] \right]. \end{aligned} \quad (\text{A8})$$

Kernels  $A_{\rho\sigma}$  are not defined at the  $k=0$  point of the reciprocal space: we set their value at this point to zero, as the electrostrictive interaction is assumed to act only on the heterogeneous part of the polarization here.

#### A.4. Dipole–dipole electrostatic force

The functional derivative of the dipole–dipole electrostatic part of the energy can be written as

$$\frac{\delta F_{\text{dep}}\{P_i\}}{\delta P_i}(\mathbf{r}) = \frac{2}{8\pi\epsilon_0\epsilon_{\mathbf{B}}} \int d^3s \left[ \frac{P_i(\mathbf{r})}{|\mathbf{R}|^3} - \frac{R_i[\mathbf{P}(\mathbf{r}) \cdot \mathbf{R}]}{|\mathbf{R}|^5} \right], \quad (\text{A9})$$

using  $\mathbf{R} = \mathbf{s} - \mathbf{r}$ . The equivalent expression for the dipole–dipole energy in reciprocal space reads

$$F_{\text{dep}}\{P_i\} = \frac{1}{8\pi\epsilon_0\epsilon_{\mathbf{B}}} \frac{\sqrt{2}}{\sqrt{\pi}} \int d^3k \left| \mathbf{P}(\mathbf{k}) \cdot \hat{\mathbf{k}} \right|^2, \quad (\text{A10})$$

and the expression sought for the Fourier space ‘force’ is obtained as

$$\mathcal{F}_d \left[ \frac{\delta F_{\text{dep}}\{P_i\}}{\delta P_i} \right] = \frac{2}{8\pi\epsilon_0\epsilon_{\mathbf{B}}} \frac{\sqrt{2}}{\sqrt{\pi}} \frac{(\mathbf{P}(\mathbf{k}) \cdot \mathbf{k})k_i}{k^2}. \quad (\text{A11})$$

The last two equations are again not defined at the origin of the reciprocal space. We define the right-hand sides of (A11) as zero at  $k=0$ , so that depolarizing field from surface charges has no influence on the final result.